APPLIED PHYSICS

Ultralight plasmonic structural color paint

Pablo Cencillo-Abad[1]*, Daniel Franklin[1,2,3,4]*, Pamela Mastranzo-Ortega[1,5], Javier Sanchez-Mondragon[5], Debashis Chanda[1,2,6]*

All present commercial colors are based on pigments. While such traditional pigment-based colorants offer a commercial platform for large-volume and angle insensitiveness, they are limited by their instability in atmosphere, color fading, and severe environmental toxicity. Commercial exploitation of artificial structural coloration has fallen short due to the lack of design ideas and impractical nanofabrication techniques. Here, we present a self-assembled subwavelength plasmonic cavity that overcomes these challenges while offering a tailorable platform for rendering angle and polarization-independent vivid structural colors. Fabricated through large-scale techniques, we produce stand-alone paints ready to be used on any substrate. The platform offers full coloration with a single layer of pigment, surface density of 0.4 g/m^2, making it the lightest paint in the world.

INTRODUCTION

Color presents one of the richest sources of sensorial information in our daily lives. Throughout history, the fascination with colors has driven human efforts to produce newer and better colorants. From the Paleolithic cave paintings to the development of the first synthetic dyes in the mid-19th century, the quest for purer, fade-resistant, and environmentally friendly colorants has remained very active. In the past decades, adding to purely decorative applications in textile, cosmetics, or food industries, colorant research has found relevance, among others, in display technologies, optical storage, sensing and therapeutics, or functional coatings (*1*, *2*).

Color engineering can be achieved by controlling the colorant's absorptive or reflective response to white light. All commercial colorants/pigments are based on absorption mechanisms. These colorants absorb photons of energies overlapping with their molecular electronic transitions. Contrarily, photons with energies not matching these discrete transitions will be reflected and registered as color by an observer. Although chemical colorants can be produced in large amounts, most of them are composed of toxic materials difficult to remove in the recycling process and are responsible for the pollution of our lifeline on earth—water (*3*). Being chemically unstable, many colorants fade with time, a process accelerated with higher temperatures or light exposure. Furthermore, as volumes of several micrometers are needed to obtain enough color saturation, they suffer from low resolution. In contrast, instead of controlling the absorption of light, structural colorants control the way the light is reflected or scattered. Structural color is the result of optical phenomena produced by micrometer- and nanoscale structures (*4*). When in bulk, the material constituents show completely different hues or are even colorless. Colors generated by engineered structures such as photonic crystals (*5*–*10*) or metasurfaces (*11*–*16*) have received increasing attention in recent years for their notable advantages over chemical colorants. Characterized by their intense brilliance and saturation, they exhibit larger stability to chemical reagents, harsh environmental conditions, and high illuminating intensities (*17*, *18*). In addition, they can offer dynamic tunability and resolutions beating the diffraction limit, both essential for display applications (*19*–*21*). Because of the geometrical nature of their response, however, structural colors usually present directional effects, i.e., their color varies with the positioning of the observer and the angle and polarization of the incident light. Many proposed architectures rely on the use of costly and low-throughput nanofabrication techniques not compatible with mass production. Overall, these constraints prohibit the commercial viability of all previously reported structural color technologies. It is therefore not surprising that, to date, no angle-independent structural paints are available in the marketplace (*22*).

Here, we present a subwavelength plasmonic cavity that overcomes these challenges while offering a tailorable platform for rendering angle and polarization-independent vivid structural colors by coupling incident light with gap plasmons. The structures are fabricated through a large-area, highly versatile, and reproducible technique where aluminum nanoislands are self-assembled in an electron beam evaporator on top of a transparent oxide-coated aluminum mirror. The optical response of these artificially engineered nanostructures can be spectrally tuned across the entire visible spectrum to form a full-color gamut by controlling the gap plasmon dispersion via the geometrical parameters. In the proposed architecture, the subwavelength optical cavity ensures a large degree of angle insensitivity, while the stochastic nature of the self-assembled layer results in polarization independence and near 100% absorption at selected spectral bands. The evaporation process, relying only on widespread industrial techniques, is compatible with many substrates and takes on their scattering properties to render diffuse and specular coloration modes when using microcorrugated or flat surfaces, respectively. E-beam evaporators are widely used in industries such as electronics, semiconductors, optics, and even aerospace, to name a few. We actually find it to be a great advantage over chemical methods, as it allows for

[1]NanoScience Technology Center, University of Central Florida, 12424 Research Parkway Suite 400, Orlando, FL 32826, USA. [2]Department of Physics, University of Central Florida, 4111 Libra Drive, Physical Sciences Bldg. 430, Orlando, FL 32816, USA. [3]Institute of Biomedical Engineering, Faculty of Applied Science and Engineering, University of Toronto, Toronto, Ontario, Canada. [4]Translational Biology and Engineering Program, Ted Rogers Center for Heart Research, Toronto, Ontario, Canada. [5]National Institute of Astrophysics, Optics, and Electronics (INAOE), Luis Enrique Erron.1, Sta. María Tonanzintla, Puebla 72840, Mexico. [6]CREOL, The College of Optics and Photonics, University of Central Florida, 4304 Scorpius St., Orlando, FL 32816, USA.
*These authors contributed equally to this work.
*Corresponding author. Email: debashis.chanda@ucf.edu

readily integration on existing production chains. Moreover, Lexus Blue, the only industrially produced structural paint, comparable to our approach, is produced using e-beam evaporators. (*23*). We present mechanisms for expanding the available color space through lateral and vertical mixing of structures, similar to traditional pigment mixing schemes. Last, to demonstrate the commercial capabilities of our platform for inorganic metallic structural coloration, we formed bidirectional structures on a water-soluble sacrificial layer that resulted in omnidirectional color flakes. These structural color flakes were then mixed with a commercial binder to develop self-standing structural color paints hundreds of times lighter than commercially available paints (*24*). Conventional chemical coloration relies on volumetric absorption of light to produce a color. In contrast to the several micrometers required for commercial paints, our ultrathin paint can impart full coloration with a thickness of only 150 nm. Consequently, this huge lateral area (few tens of micrometers)–to–thickness (100 to 150 nm) ratio makes it the lightest paint in the world with a surface density of only 0.4 g/m^2. For comparison, while a Boeing 747 requires 500 kg of paint (*25*), our ultralight paint would require about 1.3 kg, an astonishing potential about 400-fold reduction in weight (see section I of the Supplementary Materials). Our approach presents the first environmentally friendly, large-scale, multicolor, and self-standing platform for imparting nanostructured coloration to any surface, thus bridging the gap from proof of concept to industrial production.

RESULTS

Self-assembled plasmonic surface

Nature presents a rich variety of both chemical and structural coloration. For example, the pink tint of Formosa azaleas (Fig. 1A) is due to the absorption of cyaniding molecules, a type of anthocyanin pigment (*26*). In contrast, the bright metallic blue displayed by the Peruvian Morpho didius (Fig. 1B) is primarily the result of the way the blue components are scattered by the lamella nanostructures found in this butterfly's wings (*27*). Oftentimes, however, structural color in animals results from the combination of the diffraction and scattering of the outer skin layers and the molecular absorption of the complementary color by intrinsic pigments of the skin (*28*). This critical observation inspired us to produce an absorptive structural pigment where the selective absorption of specific frequencies is the result of the tailored structural resonant response of metallic nanostructures coupled to a subwavelength optical cavity. Specifically, the proposed architecture consists of a highly packed monolayer of self-assembled aluminum nanoislands on a thin aluminum oxide film that spaces them from the aluminum back mirror (Fig. 1C). In this configuration, the aluminum nanoislands resonantly absorb specific wavelengths, while the back mirror strongly back-reflects the nonresonant ones, rendering vivid colors based on colorless materials.

Contrary to other artificial structural schemes that rely on the use of low-throughput, multistep, top-down techniques such as electron beam lithography or focused ion beam, incompatible with mass production, the proposed architecture is the result of a naturally occurring nucleation process in an electron beam evaporator. In the self-assembly growth, small clusters of aluminium nanoparticles are formed due to the larger affinity of the aluminium atoms to their own kind over the oxide substrate. With a low enough rate, the evaporation of nanometric films results in a nanoparticle's monolayer that exhibits optical plasmonic resonances. Crucially, this pressure- and temperature-controlled process ensures high reproducibility over broad areas in a single step, lowering the cost of production and enabling large-scale fabrication. The dynamics of the

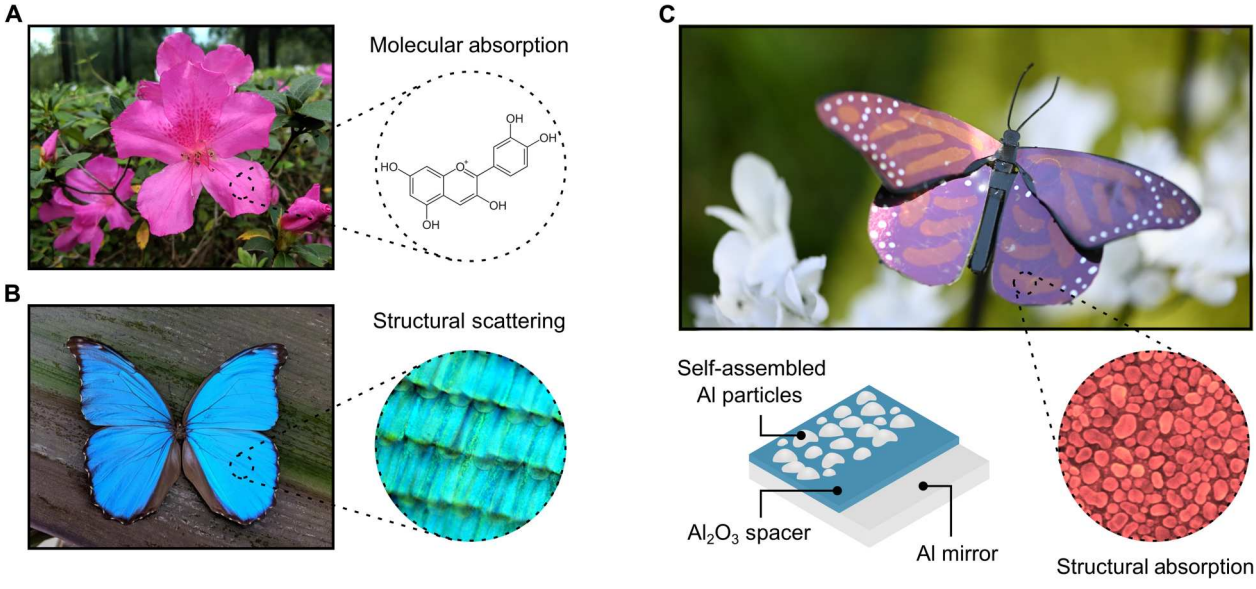

Fig. 1. Structural absorption for color generation. (**A**) Many chemical substances produce color by selectively absorbing frequencies matching their molecular electronic transitions. Pink color in Formosa azaleas is due to the absorption of cyaniding molecules. (**B**) An example of structural coloration is found in the Peruvian Morpho didius. Lamella nanostructures found in its wings scatter the blue components of incident light generating its characteristic metallic blue. (**C**) A subwavelength plasmonic cavity formed by a self-assembly of metallic nanoislands on top of an oxide-coated mirror generates color by selectively absorbing certain wavelengths and strongly back-reflecting other.

self-assembly process are presented in detail in section A of the Supplementary Materials, while the technical parameters can be found in Materials and Methods.

Optical response of the near-field coupled gap plasmons

The color produced in the nanostructure is the result of the hybridization of the absorptive response of the aluminum self-assembled monolayer, and the subwavelength cavity formed by this top layer, the aluminum back mirror, and the dielectric spacer sandwiched in between. Geometrical changes in any of the layers will then result in a change in the perceived color. When ambient light reaches the monolayer, the electric field of the light at select wavelengths can drive the free electrons of the aluminum to oscillate resonantly within the nanoparticles′ geometry. This collective oscillation, termed localized surface plasmon resonance, is further affected by the coupling between closely packed neighboring particles and the presence of the back-mirror interface at a subwavelength distance from the particles′ layer. This complex hybridization mechanism results in a gap plasmon mode that leads to strong optical absorption and tight confinement of the light at the metal/dielectric boundary of the metallic particles at resonant frequencies (*29*). The spectral position of the absorption band, and thus the perceived color, depends distinctly on the gap plasmon dispersion, which is hence controlled by three parameters: (i) the size and spatial distribution of the nanoislands, (ii) the refractive index of their environment, and (iii) the thickness of the spacing layer.

The size of the nanoislands can simply be controlled by tuning the amount of aluminum evaporated. To investigate the range of colors available with this cumulative process, we use a shutter that controls the partial exposure of the sample during the evaporation. In this manner, by rotating the sample, we can produce a polar gradient of thicknesses from 0.5 to 16 nm, in thickness increments of 0.5 nm corresponding to wedges of approximately 11° (Fig. 2B). As the thickness mass is increased, neighboring nanoislands coalesce to form larger particles (Fig. 2A, top). This increase in the nanoislands′ size red shifts the absorption band and results in different hues and saturations that produce a color palette that covers from the white of the back mirror, at very low thicknesses, to the yellow, magenta, and blue. It should be noted that being a subtractive color scheme, a red shift of the absorption band results in a blue shift in perceived color, as the intensity of blue components in the reflected light augment at the expense of the yellow and red ones. If the process is carried on for long enough, adjacent nuclei can coalesce to form semicontinuous films and, eventually, continuous films (Fig. 2A, bottom). The thickness at which the transition from isolated islands to continuous film occurs is the percolation threshold. At thicknesses above the percolation threshold, the free electrons of the metal can find paths to move through the self-assembly, eliminating the geometrical confinement necessary for the resonant plasmonic absorption and thus disabling the color production. This can be observed in the gradient wheel sample at higher thicknesses where the blue fades to white (Fig. 2B). Further details on the growth dynamics can be found in section A of the Supplementary Materials.

Together with the spectral shift, the increase in the thickness mass results in a broadening of the optical resonances. We attribute this phenomenon to the inhomogeneous broadening of the nanoparticles′ resonances arisen from the doubly random nature of both the morphology and spatial distribution, as can be seen in Fig. 3. On the one hand, as thickness mass increases, larger variability of island size can be observed (fig. S1A). To further assess this effect, we build a semianalytical model that defines the total reflection of the monolayer by weight averaging the reflection of periodic islands of 50 hemispherical radii within 4 SDs of the mean value as obtained from the SEM analysis for the 8-nm thick mass (Fig. 3A and section B of the Supplementary Materials). This larger morphological variability translates into a reduction in the reflection contrast and saturation of the colors produced, with a distinct broadening of the resonance (Fig. 3B). On the other hand, the effect of the spatial distribution can be explained by the well-known dependency of the relative position of interacting plasmonic resonators (*30*). To evaluate this latter effect, we run a set of simulations for 7 × 7 hemispherical nanoparticles, for equivalent thickness mass of 4 nm on top of a 10-nm oxide spacer, in a periodic square array, disordered array, and disordered randomized sizes (Fig. 3C). The reflection curves show additionally a spectral shift that we associate with the different energies of the new available modes resulting from the lateral hybridization of nanoparticles, modes otherwise forbidden in the symmetric arrangement (section C of the Supplementary Materials). These assumptions are confirmed from the comparison of the electric profiles in-resonance where we observe the strongly confined fields characteristic of the gap plasmon modes, for both ordered and disordered arrangements, as seen in Fig. 3D. We observe clearly that while for the ordered structure the dipolar resonance is only excited at in-resonance wavelength, both disordered and random disordered configurations show excitations even well outside the in-resonance spectral position. The inhomogeneous broadening observed is also in good agreement with the expected behavior predicted by the classical formula for dipole-dipole interaction energy given by (*28*)

$$W = k_e k_\alpha \frac{|\boldsymbol{p}_1||\boldsymbol{p}_2|}{n_e^2 |\boldsymbol{r}_{12}|^3} \quad (1)$$

where k_e is the Coulomb constant, k_α is the orientation factor, n_e is the refractive index of the environment, $|\boldsymbol{p}_1|$ and $|\boldsymbol{p}_2|$ are the moduli of the dipole moments for two interacting particles, and $|\boldsymbol{r}_{12}|$ is the modulus of the distance between them. In this near-field approximation, considering two neighbor particles interacting, if their sizes, and also shapes, show large variability, it is expected that the dipole modes corresponding to a given illuminating wavelength will be weakly excited, and consequently lower absorption will result in a poorer reflection contrast. Furthermore, the spatial disorder broadening can be understood by averaging the distance between particles, where some of them will be constructively interfering, while others will be out of phase and thus destructively interfering. Last, it should be noted that in contrast to colors produced from luminous objects, where high purity is required, our subtractive color scheme requires broad resonances to result in more saturated colors. In this case, the high-density packing of the self-assembly plays a critical role in bringing the hybridized modes to the visible range while ensuring vivid coloration in a single nanometric layer; it exacerbates the resonance broadening resulting from the dynamic depolarization of nonspherical particles (see section D of the Supplementary Materials). Although, all factors considered, spectrally purer colors could be achieved with pretreatment steps before the self-assembly growth, this would be achieved at the expense of the fabrication simplicity offered in our approach. To

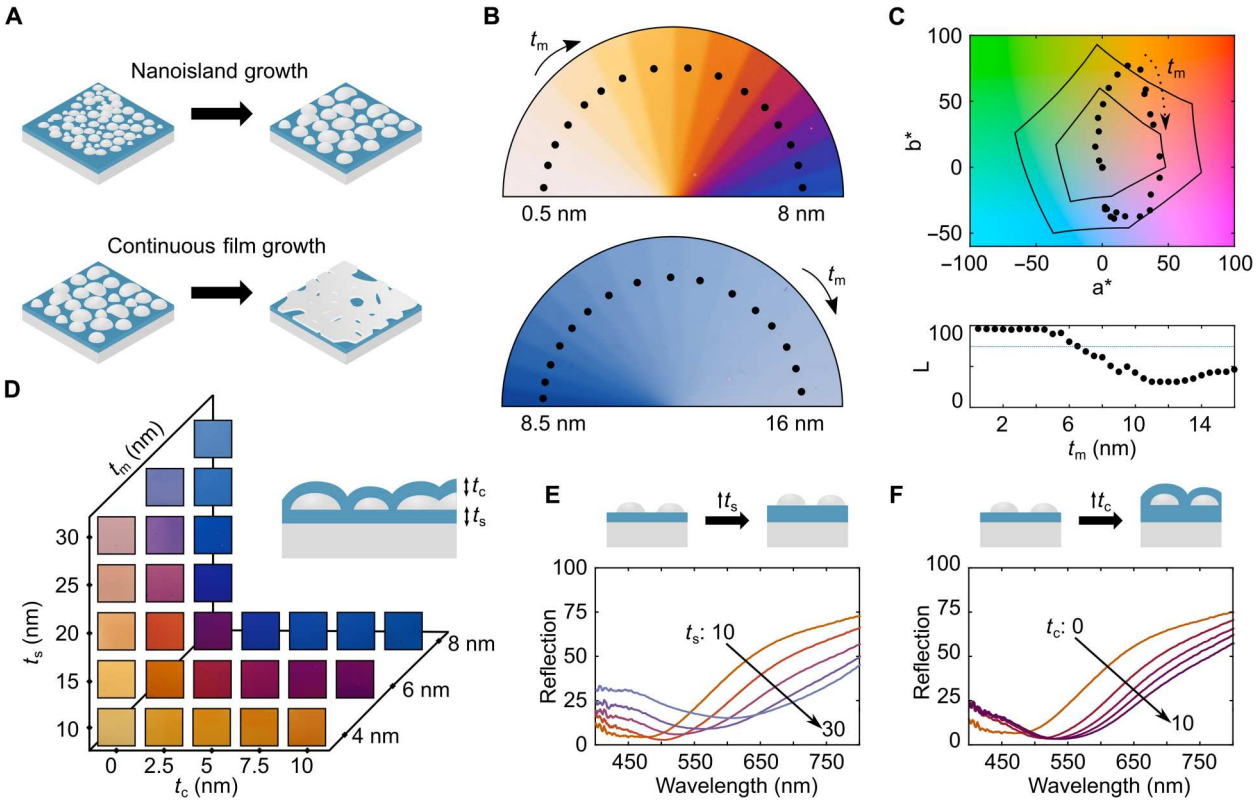

Fig. 2. Color space based on tunable gap plasmon dispersion. (**A**) In the Volmer-Weber growth mode, the size of the nanoislands can be controlled by tuning the amount of aluminum evaporated (top). If the process is carried on for long enough, semicontinuous films are formed, which disable the plasmonic resonances and thus the color (bottom). (**B**) Color polar gradient for thicknesses from 0.5 to 16 nm, for a fixed 10-nm spacer. (**C**) CIELAB coordinates for the points in the color wheel compared to ISO DIS 15339-2 cold-set newsprint and coated premium paper standards (inner and outer hexagons). (**D**) Tuning of the spacer and capping layer thicknesses expands the available color space. (**E** and **F**) The red shift of the absorption resonance as the spacer and capping layer thicknesses are increased.

better understand the coupled mechanism, we also develop a theoretical model and compared it with Finite Difference Time Domain (FDTD) simulations; the results of this can be found in section D of the Supplementary Materials.

To assess the quality of the color gamut generated by our self-assembled plasmonic structure, we calculated the L*a*b* coordinates from the reflection spectra of each thickness in the gradient sample (see Materials and Methods) and plot them as black dots in the CIELAB color space (Fig. 2C). To compare with two color quality standards used in the printing industry, we overlay the standards for the cold-set newsprint and coated premium paper technologies as defined in ISO DIS 15339-2 (inner and outer hexagon, respectively). For a substantial portion of the color space, we find that the self-assembled plasmonic color exceeds the newsprint standard and even matches the quality of some colors as produced in coated premium paper. However, although the color space of the plasmonic structure can be expanded in some regions by careful selection of the other geometrical parameters, due to its subtractive nature, the production of green is prohibited for a single-particle layer. To address this limitation, in the sections below, we introduce two different color mixing schemes.

Because of the strong field confinement in the metal-dielectric interface, plasmonic resonances are extremely sensitive to changes in the environment (*31*, *32*). The addition of a capping layer on top of the self-assembly presents an opportunity to further tune the color response by shifting the resonant spectral position of the nanoislands' layer. For samples corresponding to 4-, 6-, and 8-nm mass thicknesses and fixed 10-nm-thick oxide spacer, we monitor the color change as we grow capping layers of alumina in 2.5-nm increments (Fig. 2D). Reflection curves for the 6-nm samples can be seen in Fig. 2F. Clearly, the presence of the capping layer redshifts the plasmonic resonance producing colors with higher blue components. This behavior is captured by the classical formula for the dipole-dipole energy interaction presented in section D of the Supplementary Materials. As the thickness of the capping layer increases, more energy is contained within the higher dielectric media and the particle-particle interaction weakens. This causes lower hybridization energies and results in higher resonant wavelengths. The effect of this top layer is of particular importance from the application's point of view. Although aluminum, due to its native oxide layer, is very chemically stable in atmosphere, we found the structures to be fragile to harsh contaminants and physical contact. To address this, we capped the samples with a commercial polyurethane clear coat (DuraClear Varnish, Americana). These samples still maintained vivid colors while offering protection from physical contact and larger chemical resistance to spills as can be observed in section E of the Supplementary Materials.

The final element that controls the optical response of the structure is the spacer defined by the thickness of the transparent aluminum oxide spacer layer. As shown in Fig. 2D for samples

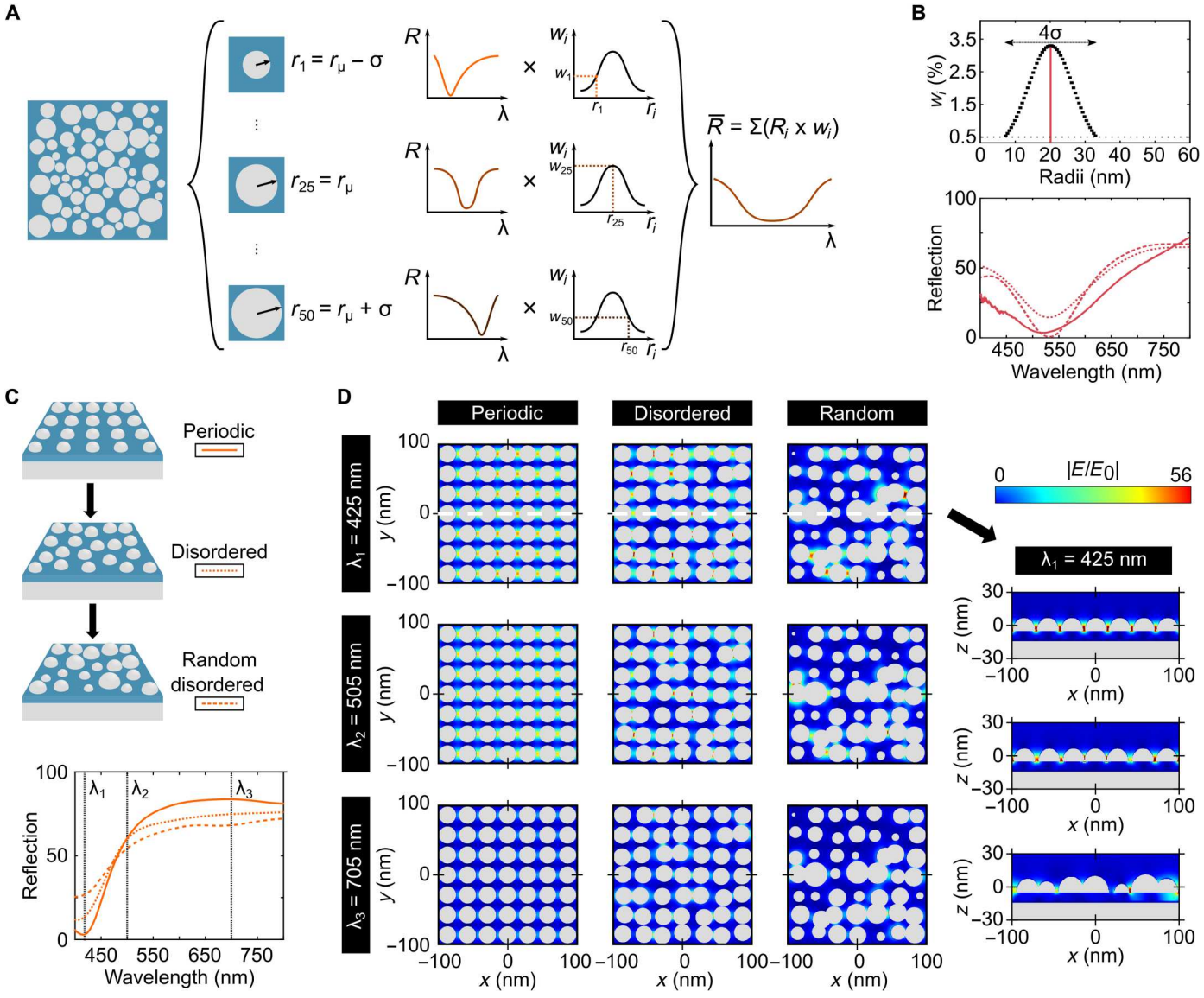

Fig. 3. Morphology effect on optical response. (**A**) The inhomogeneous broadening of the optical resonance can be accounted for by introducing size and spatial variability. We simulate the broadening by averaging the reflection curves of 50 particles with radii within 4 SDs of the mean value obtained from SEM analysis. (**B**) Statistical radii distribution (top) and reflection curves (bottom) for experimental (solid), FDTD mean value (dashed), and weight averaged (dotted). (**C**) Reflection curves for FDTD simulations corresponding to 7 × 7 hemispherical particles with equal size in periodic and disorder arrangement, and random size and disordered arrangement, equivalent to the 5-nm self-assembly. (**D**) Electric profiles in three different spectral positions as labeled in (C).

corresponding to 4-, 6-, and 8-nm mass thickness and varying spacers from 10 to 30 nm, changes in the spacer thickness result in pronounced color changes in the structure. For the 6-nm nanoparticle layer, the reflection curves are shown in Fig. 2E. We observe that as the spacer is increased, the resonance is shifted to longer wavelengths and the overall reflection levels increase producing less saturated colors. We explain the behavior of the multilayer stack using interference theory of a nonsymmetric subwavelength cavity, where the bottom mirror and the top nanostructured self-assembly form the two limiting interfaces and the ultrathin dielectric (alumina) spacer sandwiched between them that controls the vertical coupling between two metallic layers. This configuration is essential to achieve almost 100% levels of absorption in the nanostructured plasmonic self-assembled layer, which occur only when field enhancement occurs at the nanoparticle layer for wavelengths that fulfill the phase matching condition (*33*). In contrast to conventional Fabry-Perot resonators, where the phase is simply accumulated through the propagation in the dielectric and the resonant condition can only be fulfilled for cavity lengths proportional to the wavelength of light, the dispersive nature of the gap plasmon mode excited on the self-assembled Al nanoislands introduces an interface with nontrivial phase shifts and high losses that can produce absorption resonances even for deeply subwavelength thicknesses well below the resonant wavelength. As the thickness of the spacer is further increased, the mismatch between phases results in weaker absorption response and renders less saturated

colors. The different nature of this near-field coupled gap plasmon mode compared to a far-field Fabry-Perot mode is further verified for large enough spacer thicknesses. When the dielectric spacing layer takes values large enough (multiples of $\lambda/4n_s$), far-field effects become dominant and the phase accumulated through propagation can fulfill the resonant condition, as in typical Fabry-Perot resonators, resulting in a sharp dip in reflection (fig. S10). Although this resonance offers colors with higher saturation, the pure geometrical nature of the mode makes it highly angle dependent, thus limiting greatly its practical applications, offering further proof of the fundamental advantage of the near-field coupled gap plasmon engineered inside this novel self-assembled ultrathin structure, which is exploited here.

A versatile platform for structural coloration

Growing the structure with conventional evaporation techniques at low temperatures permits the use of a wide variety of substrates. To prove the versatility of the proposed plasmonic self-assembled structure, we produced multicolor butterflies by growing several stacks on wing-shaped polyethylene terephthalate (PET) templates (Fig. 4A). The polarization and angle insensitiveness of these color structures readily show their superiority over many other reported structural approaches. On the one hand, the polarization independency arises from the isotropic character of the disordered self-assembled layer, where nanoislands show no predominant direction or orientation of growth. In Fig. 4B, we show how, as expected, when photographed with unpolarized and two orthogonal linearly polarized states, the butterfly assembly shows no appreciable color difference. This particular feature of the multilayer structure is highly important for integration in devices that rely on the use of polarized light such as liquid crystal displays. On the other hand, the subwavelength character of the cavity makes the structure pretty color insensitive to the angle of incidence. Photographies of the blue artistic butterfly at three different combinations of zenith and azimuth angles show clearly that the color is retained regardless of the angle of incidence (Fig. 4C). Upon further study (section F of the Supplementary Materials), we observe the structures retaining their color for angles as large as 60°.

The adaptability to different substrates of this unique large-area, self-assembling–based fabrication method paves the path toward the integration of the stack in elastic platforms without the loss of color quality. We grow three samples with 5-, 8-, and 12-nm nanoparticle layers and fixed a 10-nm aluminum oxide spacer on top of aluminum-coated PET strips. These three configurations, corresponding to the three primaries in the CMY color mode, can be seen in Fig. 4D. Although vivid and brilliant, the specular coloration observed in flat substrates is inconvenient in many applications. For such cases, corrugated substrates can be used to produce diffuse coloration mode. In the diffuse coloration mode, careful texturing of the substrate can control the degree of dispersion of light reflected.

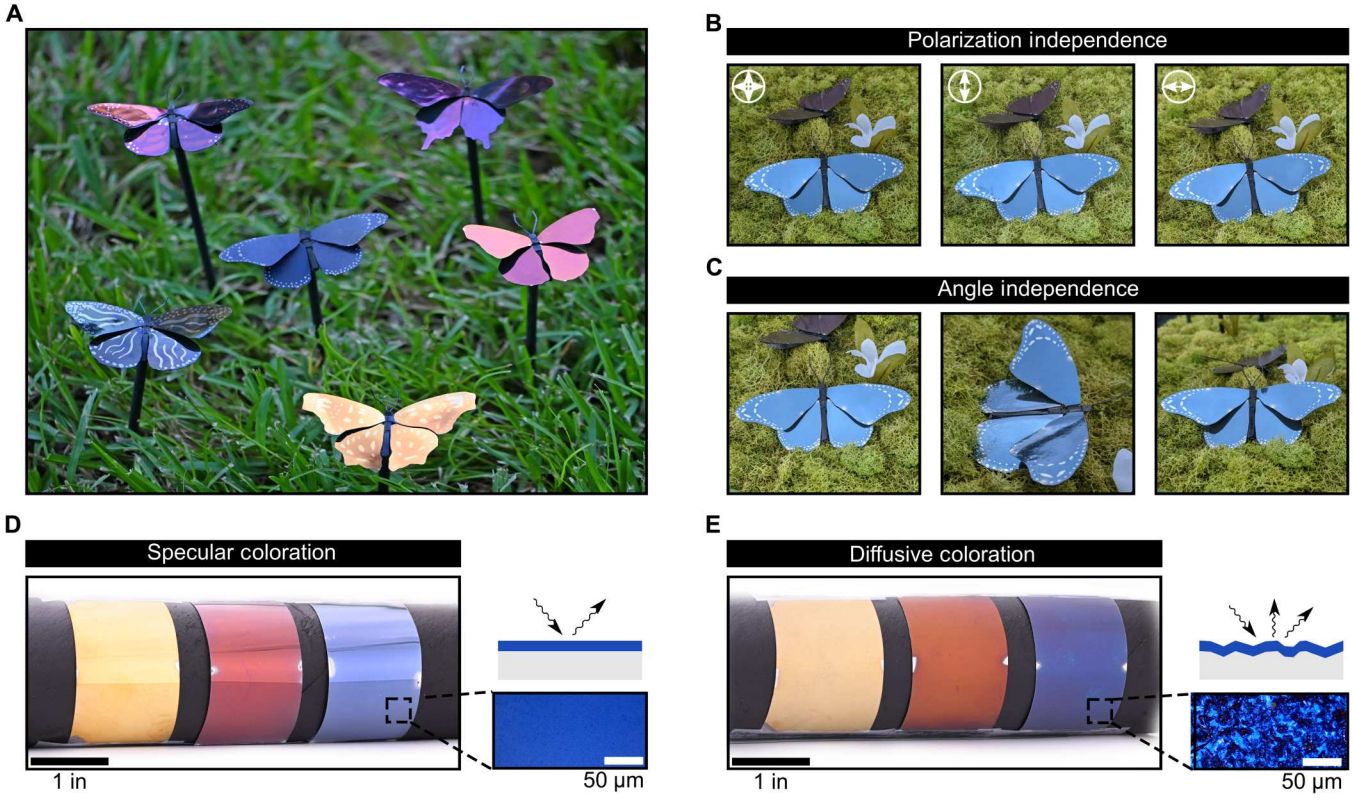

Fig. 4. Dual color mode, polarization independence, and angle insensitiveness. (**A**) Butterfly garden with an assorted collection of different butterfly wings and colors. (**B**) An artistic butterfly model coated with structural blue retains its color when photographed with unpolarized (left) and two orthogonal linearly polarized states (middle and right). (**C**) The butterfly color is also angle insensitive, as shown for three different combinations of azimuth and zenith angles. (**D** and **E**) The versatility of the self-assembly fabrication process permits the use of a wide array of substrates. Flat and sandblasted PET strips are used as flexible substrates to form the three primaries in both (D) specular and (E) diffuse coloration mode.

We produce diffuse coloration by growing the nanostack on sand-blasted PET strips (Fig. 4E). In contrast to flat substrates that result in specular coloration mode, the use of microtextured substrates results in surfaces that homogeneously diffuse the light without inconvenient light streaks of specular reflection while retaining angle and polarization insensitiveness.

Expanding the color gamut with mixing of structures

Changes in the geometrical parameters can be introduced to tailor the color response of the structure. Often, however, the production of a larger color palette is difficult, due to the limitation of primary colors. Guided by the principle of conventional color mixing where multiple pigments are mixed to produce secondary colors, we demonstrated in a unique way production of new colors by the "mixing of structures" without needing new materials. Growing side-by-side patches covered with 5- and 10-nm mass thickness nanoislands, we controlled the final color appearance by careful selection of the ratio of the area covered by each one of the particles' configurations. We define the control parameter α as the ratio of the area covered by the 10-nm equivalent nanoislands to the total area covered by both configurations (Fig. 5A). Using a lithographic mask, we define subpixels of 100-μm length and variable 0- to 100-μm width, in steps of 10 μm, to be covered by 10-nm nanoislands. The rest of the area is then covered by the 5-nm mass thickness nanoislands producing samples with α values ranging from 0 to 100. In this manner, we fabricated three samples for cavity length values of 10, 15, and 20 nm (Fig. 5B). The pixel geometry is purposely selected to be in a chessboard arrangement with pixels smaller than 100 μm to reduce chromatic aliasing and produce smooth colored surfaces to the naked eye. Microscopy insets for selected samples can be seen in Fig. 5C. This side-by-side mixing mechanism can be explained by a simple additive rule. For given reflection curves, R_A and R_B, corresponding to the two color bases A and B with mixing ratio α, the total reflection is given by

$$R_{\text{tot}} = (1 - \alpha) \cdot R_A + \alpha \cdot R_B$$

Reflection curves for the mixtures with fixed 10-nm oxide layer can be seen in Fig. 5D, where we observe the transition from one basis to the other. This is even clearer in Fig. 5E, where we have plotted as black dots the L*a*b* coordinates corresponding to the α values from 0 to 100. For context, the colorspace defined by the thickness wheel analyzed in Fig. 2C is overlaid as dotted white lines. Conveniently enough, any color contained in the segment defined by the two coordinates corresponding to the bases can be generated by careful selection of in-plane mixing ratios (section G of the Supplementary Materials).

In-plane mixing does expand the color palette by offering a route to generate any color contained in the region defined by the basis used. However, it does not permit to generate colors outside of its boundaries. Generating green shades would therefore require a green basis. Yet, due to its subtractive nature, the production of green is prohibited for the plasmonic self-assembly. However, this limitation can be broken by growing multilayers of plasmonic nanoparticles (Fig. 5F). In this multilayer configuration, two extra geometrical parameters are introduced to control the color appearance: the thickness mass of the extra layer and the interspace between the nanoisland films. We produce a wide variety of green shades by growing, on top of a base structure consisting of an aluminum mirror, 10-nm oxide layer, and 10-nm equivalent nanoislands, three top layers corresponding to 4-, 5-, and 6-nm self-assembled layers with oxide interspaces ranging from 10.5 to 22.5 nm (Fig. 5G). The reflection curves for the 5-nm equivalent top layer can be seen in Fig. 5H, while the L*a*b* coordinates for these curves are plotted as dots in Fig. 5E, where we observe how the out-of-plane mixing scheme expands the color palette to areas otherwise inaccessible with a single plasmonic layer. Although the levels of reflection in the bilayer structures are low, because of the double absorption of the twofold plasmonic layer, careful study of all geometrical parameters can help mitigate partially this effect. The interspace and top-layer geometrical parameters add to the bottom self-assembly and the spacer layer thickness to offer extra degrees of freedom to expand the available color gamut introducing new colors with different saturation and luminance (section H of the Supplementary Materials). From the industrial point of view, these new layers do not increase excessively the complexity of the manufacturing, as they can be grown in the same chamber as a single process step, with little extra time or cost. The addition of an extra plasmonic film can also be incorporated into the analytical model by adding on top of the single stack two extra layers: the dielectric interspace and an extra effective medium describing the upper plasmonic layer.

Structural color paint

The fabrication process used to grow the self-assembled structure permits an easy integration into many industrial processes that already use compatible systems. Despite this, the platform is fundamentally limited by the need to grow in situ structures. This restricts critically the applicability in contexts where nonvacuum-compatible substrates are required or instances where large areas need to be covered, as the limiting factor would always be the particular specification of the evaporation equipment used. To present a realistic alternative to commercial chemical colorants, the multilayer structure should ideally be available in a stand-alone platform that can be transferred, after fabrication, to any substrate. On top of a sacrificial layer, we evaporate sequentially a double-sided mirror–symmetric stack, where each side comprises an alumina protecting capping layer, a plasmonic self-assembly, and an alumina spacer, while the mirror is shared between them. Removal of the sacrificial layer at the end of the fabrication results in tunable self-standing doubly colored flakes (Fig. 6). We chose to grow the structures symmetrically to ensure homogeneous colorization; however, flakes can be grown in asymmetric configurations, each face showing a different color, to render new mixtures similar to the in-plane mixing color scheme explored before. Once the structures are flaked off of the substrate, the flakes can be stored dry in powder form (Fig. 6B) or kept in an organic solvent (here we used acetone; Fig. 6C). After lifting off, flakes present irregular shapes and sizes, with lateral dimensions of 20 to 150 μm. To increase homogeneity and improve efficiency when coating, a final ultrasonication and filtering step is performed to break flakes to lateral sizes of tens of micrometers (section I of the Supplementary Materials).

To demonstrate the commercial potential of this platform for inorganic metallic pigmentation, we formulated a paint by mixing the structural color flakes with a drying oil (linseed oil, Gamblin) (Fig. 6A). The mixture presents the simplest form of a paint, where the flakes are the pigment and the oil is the binder that permits transferring to the target substrate. This mixture can be used then to coat surfaces in applications otherwise incompatible

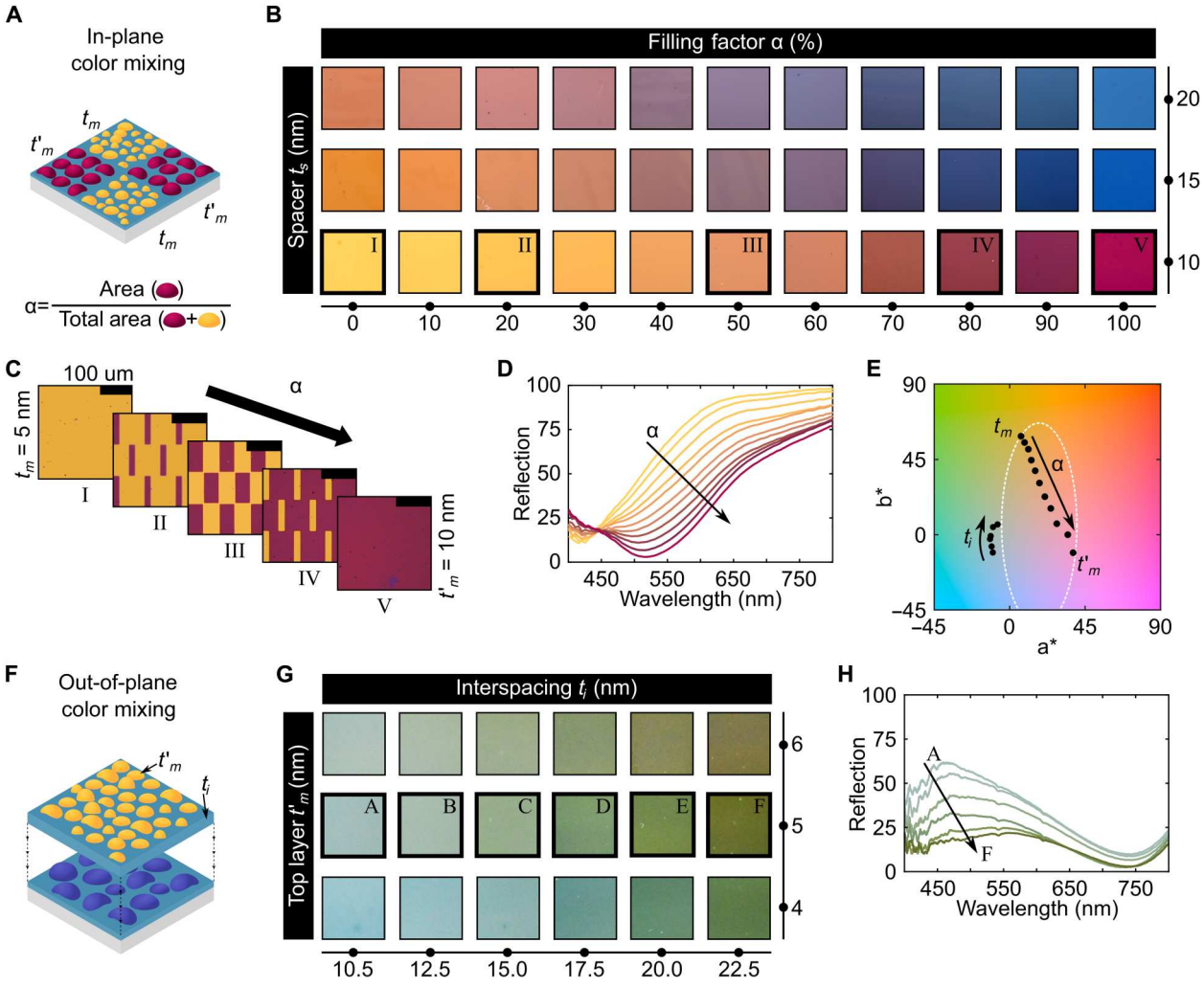

Fig. 5. Mixing of structures to expand the color gamut. (**A**) Controlling the ratio of area covered by two configurations, the reflection curve can be defined by a simple additive rule. (**B**) Camera pictures of samples with mixing ratios from 0 to 100%, for spacer thicknesses of 10, 15, and 20 nm. (**C**) Microscope images for the samples highlighted in (B). (**D**) As the ratio is increased, the reflection curves transition from pure basis A to pure basis B. (**E**) CIELAB space for the samples corresponding to spacer thickness of 10 nm in (B) and (G). The white dotted line overlay represents the space defined by the color wheel in Fig. 3C. (**F**) New colors can be generated by multilayer structures. (**G**) Green shades inaccessible with a single layer can be generated by stacking two self-assemblies with different interspacing thicknesses. (**H**) Tuning of the interspace layer between self-assemblies controls the optical response of the cavity.

with vacuum systems. In Fig. 6B, we show such an example, where we painted an artistic multicolor butterfly on a black canvas. Although different target surfaces would require more careful selection of the binder, and possibly the use of other chemical additives in the paint formulation, the structural color paint demonstrated here can be easily adapted. Provided that noncorrosive chemicals are used, the flake self-assembly structure is a universal platform independent of the particular paint components used. Last, from a commercial point of view, two additional features make this structural color paint a very promising candidate for industrial production. First, in contrast to chemical coloration schemes that use toxic and contaminant components, the fabricated flakes avoid detrimental environmental impacts by using only nontoxic materials such as aluminum and its oxide, and a biodegradable water-soluble polymer as a sacrificial layer (see Materials and Methods). Second, the structural color paint offers 100% reflection with only a single ultrathin layer of pigment (100 to 150 nm) of extremely low surface density (*22*).

DISCUSSION

While structural coloration presents a promising opportunity to substitute chemical colorants with purer and nontoxic options, commercial production of such structural color poses a challenge due to the anisotropic optical response that results in undesired effects such as dichroism or iridescence coupled with tedious fabrication processes. In this work, we have demonstrated a color nanostructure that overcomes these challenges, offering a real-world opportunity for industrial production.

Hybridizing the plasmonic response of a metallic self-assembly with an ultrathin optical cavity, we have demonstrated a large CYM palette that can be produced by simply changing the geometrical

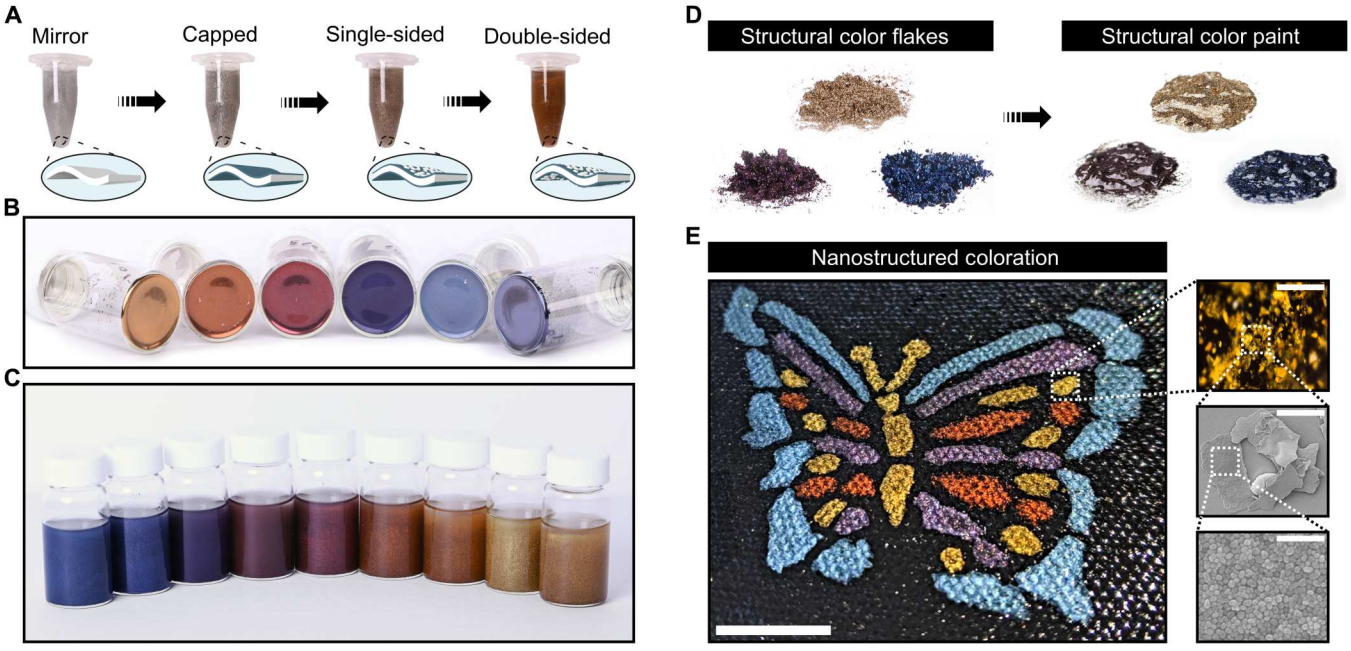

Fig. 6. Structural color paint. (**A**) Sequential growing of a bidirectional stack on a sacrificial layer results on color flakes. (**B** and **C**) Color flakes can be stored dry or dispersed in a solution. (**D**) A paint can be produced by mixing the flakes with a drying oil. This simple formulation, where the flakes are the pigments and the oil is the binder, can be adapted to impart the nanostructured coloration to any surface. (**E**) Photography of a multicolor artistic butterfly on a black canvas painted with a set of linseed oil–based plasmonic paints demonstrating the commercial feasibility of the platform. Insets correspond to a microscope image (top) and SEM micrographs (bottom). Scale bar for the butterfly is 1 inch, whereas for the insets, from top left to bottom right, scale bars correspond to 1 mm, 100 μm, 75 μm, and 100 nm, respectively.

parameters of the structure. Furthermore, we studied mechanisms for expanding the available color space through multilayers and in-plane addition for cost-effective color mixing to expand the color gamut further. While the isotropic character of the nanoislands′ layer ensures polarization independence, the angle insensitiveness, otherwise impossible in conventional Fabry-Perot resonators, is achieved by exploiting the nontrivial phase discontinuities in the ultrathin cavity, thus avoiding path length effects for steep angles close to 70°.

The subwavelength plasmonic cavity is fabricated with a low-temperature process in an e-beam evaporator. The versatility of the process permits the use of many different substrates, including flexible platforms required in wearable electronics and roll-to-roll manufactures, and takes on the scattering properties of the target surface to produce both diffuse and specular coloration mode. In addition, being a self-assembly process, the color consistency is ensured for large areas. We observed that color purity of our structure is dependent on the size and shape distribution of the nanoislands. We note that although the use of preseeding techniques, higher temperatures, or alternative materials would improve control o the assembly morphology, it would impose a scale and cost toll on the manufacturing process.

To demonstrate the commercial capabilities of our platform for inorganic metallic pigments, we have fabricated self-standing bidirectional color flakes by evaporating on top of a water-soluble sacrificial layer a double-sided stack. This ultralight pigment, which offers full coloration with a single layer of flakes, can then be mixed with a binder matrix to formulate a structural color paint that can be used to coat, after fabrication, any surface. With an unbeatable surface density of 0.4 g/m2, hundreds of times lighter than commercially available paints, this approach presents an ultralight, multicolor, large-scale, low-cost, and environmentally friendly platform for imparting nanostructured coloration to any surface, thus paving the way toward industrial production and real-world application.

MATERIALS AND METHODS

Self-assembled structural color fabrication

The optically thick back mirror is produced by evaporating 100 nm of aluminum on a Thermionics e-beam evaporator. Pressure at the beginning of the evaporation was ~1×10^{-6} torr, and evaporation rate was kept at 0.1 nm/s. A spacer layer of aluminum oxide was then grown by atomic layer deposition (Savannah 200, Cambridge Nanotech) by pulsing trimetylaluminum and water at 100°C. The aluminum nanoparticles were then produced on an Ultra High Vacuum electron beam evaporator (AJA International). In agreement with previous studies (*20*, *34*–*36*), we find that three parameters play a critical role in the geometry of the self-assembled monolayer: the temperature of the substrate, the pressure in the chamber, and the rate of growth. We chose these parameters compromising between the desired higher saturation of colors and the lower requirements for fabrication that ensures the versatility of the proposed architecture and the viability of a transition to industrial-scale production. Thus, we chose to keep the temperature of the substrates at 100°C, resulting in high color saturation while being below the melting point of many polymers, essential for flexible substrate applications and lift-off during flake preparation. For reproducibility and color vividness, nanoparticles′ growth was carried on at pressures below 5×10^{-8} torr, while

growth rates were kept constant at about 0.1 A/s, both readily available in conventional UHV evaporators. It should be noted that although an atomic layer deposition (ALD) system was used for convenience for the hard substrates, the entire fabrication process could be carried on in a single UHV e-beam evaporator. To prove this promising ease of integration, critical for industrial chain systems, the oxide layer in the pigment flake production was grown at room temperature on the Thermionics e-beam evaporator system. Besides a slight change in color shade, attributed to the change in refractive index of the oxide layer, no fundamental quality change was observed between the layers grown by the two systems. Last, we note that while many other metals and dielectrics have been explored to produce an even larger color gamut, to emphasize the practicality of the approach, we report here only the ones produced using aluminum and its oxide, as we find it the optimal solution from a fabrication and cost point of view.

Finite difference time domain modeling

The reflection spectra and electric field distribution of the simulated samples were calculated using the experimental geometrical parameters extracted from the scanning electron microscopy (SEM) analysis of the samples, with a commercial FDTD software package (Lumerical FDTD, Lumerical Solutions Inc.). The relative permittivities of aluminum and aluminum oxide are taken from literature (*37*). To build the weight-averaged semianalytical model of fig. S2, we simulated a single particle with periodic conditions. The values of the unit cell size were chosen to make the area covered by the aluminum island equivalent to those obtained from the SEM analysis for the different samples (55, 60, and 70% for 4, 8, and 12 nm, respectively). Fifty simulations with radii values within 4 SDs of the mean value were then performed, and the weight-averaged reflectance was calculated as

$$\overline{R} = \sum_i R_i \times w_i$$

where w_i and R_i represent the Gaussian weight and simulated reflection for the particle *i*. For the analysis of the effect of the disorder as shown in fig. S3, we simulated an array of 49 particles placed in periodic arrangement, disordered arrangement, and disordered arrangement of different radii, introducing the disorder parameter following the method presented by Zhang and colleagues (*38*).

Color gamut evaluations

To find the L*a*b* coordinates of the fabricated samples, we first obtained the XYZ tristimulus values integrating over the visible spectrum according to

$$X = \frac{1}{N}\int \overline{x}(\lambda)R(\lambda)I(\lambda)d\lambda$$

$$Y = \frac{1}{N}\int \overline{x}(\lambda)R(\lambda)I(\lambda)d\lambda$$

$$Z = \frac{1}{N}\int \overline{x}(\lambda)R(\lambda)I(\lambda)d\lambda$$

$$N = \int \overline{y}(\lambda)I(\lambda)d\lambda$$

where $R(\lambda)$ is the measured reflectance; $\overline{x}(\lambda)$, $\overline{y}(\lambda)$, and $\overline{z}(\lambda)$ are the color matching functions; and $I(\lambda)$ is the reference illuminant. From the tristimulus values CIEXYZ, the CIELAB coordinates can be calculated from

$$L^* = 116\, f_y - 16$$

$$a^* = 500\ (f_x - f_y)$$

$$b^* = 200\ (f_y - f_z)$$

where, being $t_x = \frac{X}{X_n}$, $t_y = \frac{Y}{Y_n}$, or $t_z = \frac{Z}{Z_n}$, and $X_N = 0.9642$, $Y_N = 1.0000$, and $Z_N = 0.8251$, the D50 white point coordinates

$$f_i = \begin{cases} \sqrt{[3]}{t_i} & \text{if } t > \left(\frac{6}{29}\right)^3 \\ \frac{841}{108}\, t_i + \frac{4}{29} & \text{otherwise} \end{cases}$$

As the reference illuminant, we chose D50, used in the graphic arts industry for color proofing as per ISO 3664:2009. Last, to keep consistency, all colormaps presented in the figures in the main manuscript and the Supplementary Materials correspond to a horizontal slice with $L^* = 75$.

Measurements and images

Reflection measurements were taken at normal incidence with unpolarized light using a 4×, 0.07–numerical aperture objective and a fiber-coupled spectrometer (HR 2000+, Ocean Optics). An aluminum mirror was used as a reference. Angular measurements were taken with an integrating sphere (RTC-060-SF, Labsphere) connected to the spectrometer. To ensure consistency in illumination, the samples were photographed with flashlight at fixed intensity. Photographies for the butterfly models were taken under sun illumination with a linear polarizer attached to the objective.

Supplementary Materials

This PDF file includes:

Supplementary Text
Figs. S1 to S17
References

REFERENCES AND NOTES

1. H. Mustroph, Dyes, General Survey, in *Ullmann's Encyclopedia of Industrial Chemistry* (American Cancer Society, 2014), pp. 1–38.
2. P. Gregory, *High-Technology Applications of Organic Colorants* (Springer US, 1991).
3. E. Brillas, C. A. Martínez-Huitle, Decontamination of wastewaters containing synthetic organic dyes by electrochemical methods. An updated review. *Appl. Catal. B* **166–167**, 603–643 (2015).
4. N. Dushkina, A. Lakhtakia, Structural colors, in *Engineered Biomimicry*, A. Lakhtakia, R. J. Martín-Palma, Eds. (Elsevier, 2013), pp. 267–303.
5. A. C. Arsenault, D. P. Puzzo, I. Manners, G. A. Ozin, Photonic-crystal full-colour displays. *Nat. Photonics* **1**, 468–472 (2007).
6. H. Kim, J. Ge, J. Kim, S. E. Choi, H. Lee, H. Lee, W. Park, Y. Yin, S. Kwon, Structural colour printing using a magnetically tunable and lithographically fixable photonic crystal. *Nat. Photonics* **3**, 534–540 (2009).
7. M. G. Han, C. G. Shin, S.-J. Jeon, H. Shim, C.-J. Heo, H. Jin, J. W. Kim, S. Lee, Full color tunable photonic crystal from crystalline colloidal arrays with an engineered photonic stop-band. *Adv. Mater.* **24**, 6438–6444 (2012).
8. H. Wang, K.-Q. Zhang, Photonic crystal structures with tunable structure color as colorimetric sensors. *Sensors (Basel)* **13**, 4192–4213 (2013).

9. H. S. Lee, T. S. Shim, H. Hwang, S.-M. Yang, S.-H. Kim, Colloidal photonic crystals toward structural color palettes for security materials. *Chem. Mater.* **25**, 2684–2690 (2013).
10. D. H. Kim, Y. J. Yoo, J. H. Ko, Y. J. Kim, Y. M. Song, Standard red green blue (sRGB) color representation with a tailored dual-resonance mode in metal/dielectric stacks. *Opt. Mater. Express* **9**, 3342–3351 (2019).
11. J. Zhang, J.-Y. Ou, K. F. MacDonald, N. I. Zheludev, Optical response of plasmonic relief meta-surfaces. *J. Opt.* **14**,114002(2012).
12. S. J. Tan, L. Zhang, D. Zhu, X. M. Goh, Y. M. Wang, K. Kumar, C. W. Qiu, J. K. W. Yang, Plasmonic color palettes for photorealistic printing with aluminum nanostructures. *Nano Lett.* **14**, 4023–4029 (2014).
13. S. Sun, Z. Zhou, C. Zhang, Y. Gao, Z. Duan, S. Xiao, Q. Song, All-dielectric full-color printing with TiO_2 metasurfaces. *ACS Nano* **11**, 4445–4452 (2017).
14. X. Zhu, W. Yan, U. Levy, N. A. Mortensen, A. Kristensen, Resonant laser printing of structural colors on high-index dielectric metasurfaces. *Sci. Adv.* **3**, e1602487 (2017).
15. J. Jang, T. Badloe, Y. Yang, T. Lee, J. Mun, J. Rho, Spectral modulation through the hybridization of Mie-scatterers and quasi-guided mode resonances: Realizing full and gradients of structural color. *ACS Nano* **14**, 15317–15326 (2020).
16. T. Badloe, J. Kim, I. Kim, W.-S. Kim, W. S. Kim, Y.-K. Kim, J. Rho, Liquid crystal-powered Mie resonators for electrically tunable photorealistic color gradients and dark blacks. *Light Sci. Appl.* **11**, 118 (2022).
17. A. S. Roberts, A. Pors, O. Albrektsen, S. I. Bozhevolnyi, Subwavelength plasmonic color printing protected for ambient use. *Nano Lett.* **14**, 783–787 (2014).
18. F. Cheng, J. Gao, T. S. Luk, X. Yang, Structural color printing based on plasmonic metasurfaces of perfect light absorption. *Sci. Rep.* **5**, 11045 (2015).
19. K. Kumar, H. Duan, R. S. Hegde, S. C. W. Koh, J. N. Wei, J. K. W. Yang, Printing colour at the optical diffraction limit. *Nat. Nanotechnol.* **7**, 557–561 (2012).
20. D. Franklin, Z. He, P. Mastranzo Ortega, A. Safaei, P. Cencillo-Abad, S.-T. Wu, D. Chanda, Self-assembled plasmonics for angle-independent structural color displays with actively addressed black states. *Proc. Natl. Acad. Sci. U.S.A.* **117**, 13350–13358 (2020).
21. Q. Hu, K.-T. Lin, H. Lin, Y. Zhang, B. Jia, Graphene metapixels for dynamically switchable structural color. *ACS Nano* **15**, 8930–8939 (2021).
22. S. D. Rezaei, Z. Dong, J. Y. E. Chan, J. Trisno, R. J. H. Ng, Q. Ruan, C.-W. Qiu, N. A. Mortensen, J. K. W. Yang, Nanophotonic structural colors. *ACS Photonics* **8**, 18–33 (2021).
23. Toyota Motor Corporation, The All-New Lexus LC Structural Blue Edition; www.lexus.eu/discover-lexus/lexus-news/lc-structural-blue.
24. D. Stoye, W. Freitag, *Paints, Coatings and Solvents: Second, Completely Revised Edition* (Wiley Blackwell, ed. 2, 2007).
25. The Boeing Company, Painting versus Polishing of Airplane Exterior Surfaces; www.boeing.com/commercial/aeromagazine/aero_05/textonly/fo01txt.html.
26. S. Asen, P. S. Budin, Cyanidin 3-arabinoside-5-glucoside, an anthocyanin with a new glycosidic pattern, from flowers of "Red Wing" azaleas. *Phytochemistry* **5**, 1257–1261 (1966).
27. S. Kinoshita, S. Yoshioka, K. Kawagoe, Mechanisms of structural colour in the Morpho butterfly: Cooperation of regularity and irregularity in an iridescent scale. *Proc. R. Soc. Lond. B Biol. Sci.* **269**, 1417–1421 (2002).
28. S. Kinoshita, S. Yoshioka, Structural colors in nature: The role of regularity and irregularity in the structure. *ChemPhysChem* **6**, 1442–1459 (2005).
29. S. A. Maier, *Plasmonics: Fundamentals and Applications* (Springer, 2007).
30. U. Kreibig, M. Vollmer, *Optical Properties of Metal Clusters* (Springer, 1995).
31. G. Schmidl, J. Dellith, H. Schneidewind, D. Zopf, O. Stranik, A. Gawlik, S. Anders, V. Tympel, C. Katzer, F. Schmidl, W. Fritzsche, Formation and characterization of silver nanoparticles embedded in optical transparent materials for plasmonic sensor surfaces. *Mater. Sci. Eng. B* **193**, 207–216 (2015).
32. K. M. Mayer, J. H. Hafner, Localized surface plasmon resonance sensors. *Chem. Rev.* **111**, 3828–3857 (2011).
33. M. A. Kats, F. Capasso, Optical absorbers based on strong interference in ultra-thin films. *Laser Photon. Rev.* **10**, 735–749 (2016).
34. T. Andersson, C. G. Granqvist, Morphology and size distributions of islands in discontinuous films. *J. Appl. Phys.* **48**, 1673 (2008).
35. M. Lončarić, J. Sancho-Parramon, M. Pavlović, H. Zorc, P. Dubček, A. Turković, S. Bernstorff, G. Jakopic, A. Haase, Optical and structural characterization of silver islands films on glass substrates. *Vacuum* **84**, 188–192 (2009).
36. J. H. Ko, S. H. Kim, M. S. Kim, S. Y. Heo, Y. J. Yoo, Y. J. Kim, H. Lee, Y. M. Song, Lithography-free, large-area spatially segmented disordered structure for light harvesting in photovoltaic modules. *ACS Appl. Mater. Interfaces* **14**, 44419–44428 (2022).
37. E. D. Palik, *Handbook of Optical Constants of Solids* (Academic Press, 1998), vol. 3.
38. P. Mao, C. Liu, F. Song, M. Han, S. A. Maier, S. Zhang, Manipulating disordered plasmonic systems by external cavity with transition from broadband absorption to reconfigurable reflection. *Nat. Commun.* **11**, 1538 (2020).
39. R. W. Vook, Nucleation and growth of thin films. *Opt. Eng.* **23**, 343–348 (1984).
40. J. A. Venables, G. D. T. Spiller, Nucleation and growth of thin films. *NATO Adv. Stud. Inst. Ser.* **86**, 341–404 (1983).
41. F. Ruffino, M. G. Grimaldi, Detailed investigation of the influence of the process parameters on the nano-morphology of Ag deposited on SiC by radio-frequency sputtering. *J. Appl. Phys.* **110**, 044311 (2011).
42. N. Kaiser, Review of the fundamentals of thin-film growth. *Appl. Optics* **41**, 3053–3060 (2002).
43. W. Gotschy, K. Vonmetz, A. Leitner, F. R. Aussenegg, Thin films by regular patterns of metal nanoparticles: Tailoring the optical properties by nanodesign. *Appl. Phys. B* **63**, 381–384 (1996).
44. J. A. Floro, S. J. Hearne, J. A. Hunter, P. Kotula, E. Chason, S. C. Seel, C. V. Thompson, The dynamic competition between stress generation and relaxation mechanisms during coalescence of Volmer–Weber thin films. *J. Appl. Phys.* **89**, 4886–4897 (2001).
45. J. Schindelin, I. Arganda-Carreras, E. Frise, V. Kaynig, M. Longair, T. Pietzsch, S. Preibisch, C. Rueden, S. Saalfeld, B. Schmid, J.-Y. Tinevez, D. J. White, V. Hartenstein, K. Eliceiri, P. Tomancak, A. Cardona, Fiji: An open-source platform for biological-image analysis. *Nat. Methods* **9**, 676–682 (2012).
46. C. F. Bohren, D. R. Huffman, *Absorption and Scattering of Light by Small Particles* (Wiley, 1998).
47. J. J. Mock, M. Barbic, D. R. Smith, D. A. Schultz, S. Schultz, Shape effects in plasmon resonance of individual colloidal silver nanoparticles. *J. Chem. Phys.* **116**, 6755–6759 (2002).
48. K. L. Kelly, E. Coronado, L. L. Zhao, G. C. Schatz, The optical properties of metal nanoparticles: The influence of size, shape, and dielectric environment. *J. Phys. Chem. B* **107**, 668–677 (2002).
49. S. Sheikholeslami, Y.-W. Jun, P. K. Jain, A. P. Alivisatos, Coupling of optical resonances in a compositionally asymmetric plasmonic nanoparticle dimer. *Nano Lett.* **10**, 2655–2660 (2010).
50. M. Born, E. Wolf, *Principles of Optics* (Cambridge Univ. Press, 1999).
51. W. S. Jodrey, E. M. Tory, Computer simulation of close random packing of equal spheres. *Phys. Rev. A* **32**,2347(1985).
52. E. M. Tory, B. H. Church, M. K. Tam, M. Ratner, Simulated random packing of equal spheres. *Can. J. Chem. Eng.* **51**, 484–493 (1973).
53. V. A. Fedotov, V. I. Emel'yanov, K. F. MacDonald, N. I. Zheludev, Optical properties of closely packed nanoparticle films: Spheroids and nanoshells. *J. Opt. A Pure Appl. Opt.* **6**, 155 (2003).
54. R. Woodbridge, *Principles of Paint Formulation* (Springer, 1991).
55. The Boeing Company, Boeing: 747-8;www.boeing.com/commercial/747/.

Acknowledgments

Funding: This work at the University of Central Florida was supported by NSF grant no. ECCS-1920840. P.C.-A. acknowledges the support from the UCF Preeminent Postdoctoral Fellowship Program (P3). **Author contributions:** Research design and conceptualization: P.C.-A., D.F., and D.C. Investigation: P.C.-A., P.M.-O., and D.F. Data analysis: P.C.-A. Writing: P.C.-A. and D.C. Overview: P.C.-A., J.S.-M., and D.C. **Competing interests:** D.C. and D.F. are coinventors on a patent application filed by the University of Central Florida (no. 2020/0181421; published on 11 June 2020). The authors declare that they have no other competing interests. **Data and materials availability:** All data needed to evaluate the conclusions in the paper are present in the paper and/or the Supplementary Materials.

Submitted 9 November 2022
Accepted 2 February 2023
Published 8 March 2023
10.1126/sciadv.adf7207